Graz University of Technology
Institute of Applied Mechanics

Preprint Series

Preprint No 02/2011

A Symmetric Galerkin Boundary Element Method for 3d Linear Poroelasticity

Michael Messner, Martin Schanz
Institute of Applied Mechanics, Graz University of Technology

Published in: *Acta Mechanica*, 223(8), 1751–1768, 2012
DOI 10.1007/s00707-012-0637-9

Latest revision: June 30, 2011

Abstract

In this paper a symmetric Galerkin boundary element formulation for 3D linear poroelasticity is presented. By means of the Convolution Quadrature Method the time domain problem is decoupled into a set of Laplace domain problems. Regularizing their kernel functions via integration by parts, it is possible to compute all operators for rather general discretizations, only requiring the evaluation of weakly singular integrals. At the end some numerical results are presented and compared with a collocation BEM. Throughout these studies, the symmetric Galerkin BEM performs better than the collocation method, especially for not optimal discretizations parameters, i.e. a bad relation of mesh to time-step size. The most obvious advantages can be observed in the fluid flux results. However, these advantages are obtained at a higher numerical cost.

1 Introduction

Biot's theory of linear poroelasticity describes a coupled system of a linear elastic isotropic material with an acoustic one. Since this is a linear theory, boundary element methods can be used for the numerical simulation of problems exhibiting such properties, e.g. wave propagation in soil mechanics, geophysics, petroleum industry and so on.

In this article a symmetric Galerkin (SG) approach is chosen, even though talking about engineering applications before. This is motivated by the fact that for a realistic simulation of such applications often a coupling with, e.g. finite element methods (FEM) is required. The SG scheme applied within this paper is not only advantageous with respect to this coupling [8], but also known for having nicer properties in general compared to other formulations [6], e.g. theoretical properties from operator theory apply in a rather natural fashion. Moreover, since the simplest description of a poroelastic material in a closed form is only available in either frequency or Laplace domain, the convolution quadrature method (CQM) [14, 15] is the natural choice to be used for the discretization of the arising time convolution when working with boundary integral equations. For this scheme a Laplace domain description of the problem is sufficient to overcome the drawback of a practically missing time domain fundamental solution. This leads to the proposed CQM-based SGBEM for mixed initial boundary value problems in linear poroelasticity. As a good introduction to symmetric Galerkin boundary element methods the paper by Bonnet et al. [6] is recommended. It gives a good overview including the general advantages of SGBEMs over collocation BEMs (CBEM). On the other hand, the paper by Schanz [22] may serve as a good introduction to linear poroelasticity.

Using the second boundary integral equation (BIE) for the SG formulation involves the hypersingular operator (HSO), for which it is troublesome to find a meaningful implementation. In the two separated fields, potential problems on one side and linear elasticity on the other one, there are different regularization strategies available, which one may hope to be able to transfer to the combined problem of linear poroelasticity. To give a short overview, these approaches are split into three different categories: *Analytical integration*, e.g. [25], the first of whom, is limited to only a few types of shape functions. This is a rather strong restriction when looking for a general implementation. Then, there are *numerical schemes*, e.g. [9] – based on the fact that the difference between a steady state and the corresponding transient fundamental solution is regular. This approach is more general than the previous one, however, from a numerical stability point of view, such differences should be avoided. Finally, there are strategies relying on *integration by parts*, which contrary to the previous approach, treat the kernel as a whole. Chronologically, Maue [17] was the first one to present a regularization for the Laplace equation, even before the other two strategies had appeared. This may be motivated by the fact that his regularization is performed on an analytical level and was not developed for a pure numerical purpose. The same holds for linear elastostatics, where already Kupradze [13] provided all essential ingredients for the regularization later presented by Han [10]. These advantages, together with the fact that throughout the regularization of the HSO one also obtains a regularization for the double layer operator, are in favor of this last approach. Therefore, the initially mentioned observation that the singularity of the steady state fundamental solution carries over to the transient one, is stressed again. However, in this case not a difference is involved, but the procedure is simply extended to the dynamic case as, e.g. it has been done in [11] for 3d-linear elastodynamics.

The same strategy can be used for linear poroelasticity, where the Laplace domain fundamental solution required within a CQM-based time discretization can be decomposed such that the regularization of the fluid part follows [26] and for the solid part the procedure from [10] is adopted.

While so far all BE formulations in linear poroelasticity were based on the first BIE – Manolis and Beskos [16] got time domain results via an inverse Laplace transformation, Wiebe and Antes [27] established a reduced BE formulation in time domain and Schanz [21] introduced a CQM-based scheme – here, for the first time the second BIE has been incorporated into the simulation of linear poroelastic problems by means of an SGBEM. Simultaneously, Schanz et al. [24] did all the mathematical proofs for this formulation, some of which will be validated in the numerical examples section, also a novelty in the context of linear poroelasticity and boundary element methods. Even though Schanz et al. [24] showed 'optimality' of the SG formulation, it will be interesting to compare this formulation with the previously established collocation BEM formulation of the authors Messner and Schanz [18] themselves. In some sense, this article may even be conceived as a finalization of this previous work. Thus, for a better understanding it is strongly recommended to have [18] at hands, because it will repeatedly be referred to throughout this paper.

Notation Operator notation is used throughout the article, with only a few exceptions, where operations are written out component wise. $\hat{(\cdot)}$ is used to identify the Laplace transform of a quantity, whereas $(\cdot)$ in general either belongs to time domain or is time independent at all. For Euclidean coordinates coordinates $\tilde{x}, x, y$ are used, while elements of physical fields are denoted by bold lower case letters. Upper case letters are reserved for the fundamental solution. In general, bold letters are used to mark tensorial quantities, where the order should be clear from the context.

2 Problem Statement in Laplace Domain

2.1 Biot's Theory

Considering a linearized three-dimensional setting, Biot's theory [3, 4] leads to a set of second order partial differential equations describing the state of a saturated poroelastic continuum in some domain $\Omega \subset \mathbb{R}^3$ for all times $t \in \mathbb{R}^+$.

However, having the later use of the CQM in mind, it is not only efficient but also sufficient [5] to state the $(\hat{\mathbf{u}}, \hat{p})$ - formulation in Laplace domain with $s \in \mathbb{C}^{R+} := \{\mathbb{C} \,|\, \Re(s) \geq 0\}$. Assuming homogeneous initial conditions, a homogeneous mixed boundary value problem (BVP) in linear poroelasticity in terms of the generalized displacement field $\hat{\mathbf{u}}^g = (\hat{\mathbf{u}}, \hat{p})^\top$ is stated by

$$\begin{aligned} \hat{\mathcal{L}}_{\tilde{x}} \hat{\mathbf{u}}^g(\tilde{x}) &= \mathbf{0} && \forall\, \tilde{x} \in \Omega \\ \hat{\mathbf{u}}^g(x) &= \hat{\mathbf{g}}^D && \forall\, x \in \Gamma_D \\ \hat{\mathbf{t}}^g(x) &= \hat{\mathbf{g}}^N && \forall\, x \in \Gamma_N\,. \end{aligned} \tag{1}$$

The differential operator is defined by

$$\hat{\mathcal{L}}_{\tilde{x}} = \begin{bmatrix} \mathcal{L}^s_{\tilde{x}} + s^2(\rho - \beta\rho^f)\, I & (\alpha-\beta)\nabla_{\tilde{x}} \\ s(\alpha-\beta)\nabla^\top_{\tilde{x}} & \frac{\beta}{s\rho^f}\mathcal{L}^f_{\tilde{x}} + \frac{s\phi^2}{R} \end{bmatrix} \tag{2}$$

and the generalized tractions by

$$\hat{\mathbf{t}}^g(x) := \begin{bmatrix} \hat{\mathbf{t}}(x) \\ \hat{q}(x) \end{bmatrix} = \lim_{\Omega \ni \tilde{x} \to x \in \Gamma} \hat{\mathcal{T}}_{\tilde{x}} \hat{\mathbf{u}}^g(\tilde{x}) := \lim_{\Omega \ni \tilde{x} \to x \in \Gamma} \begin{bmatrix} \mathcal{T}^s_{\tilde{x}} & -\alpha \mathbf{n}_x \\ s\beta \mathbf{n}_x^\top & \frac{\beta}{s\rho^f}\frac{\partial}{\partial \mathbf{n}_{\tilde{x}}} \end{bmatrix} \begin{bmatrix} \hat{\mathbf{u}}(\tilde{x}) \\ \hat{p}(\tilde{x}) \end{bmatrix}. \tag{3}$$

$\mathcal{L}^s_{\tilde{x}}$ is the differential operator of linear elastostatics and $\mathcal{T}^s_{\tilde{x}} = \lambda \mathbf{n}_x \nabla^\top_{\tilde{x}} + \mu\left(\nabla_{\tilde{x}} \mathbf{n}_x^\top + \nabla^\top_{\tilde{x}} \mathbf{n}_x\right)$ its Neumann trace reflecting Hooke's law (λ, μ are the Lamé constants). Furthermore, ρ is the bulk density and ρ^f the fluid density. Biot's effective stress coefficient is introduced as $\alpha = \phi\,(1 + Q/R)$ with the porosity ϕ and the factors Q and R describing the coupling between fluid and solid. Finally, the factor $\beta = \beta(s, \kappa, \phi, \rho^f)$ additionally depends on the permeability κ.

Remark 1. *Note that with this definition of the Neumann trace* (3)*, the inward flux is positive. Since the classical sign convention is opposite, its sign will be reverted in the final results.*

2.2 Boundary Integral Formulation

2.2.1 Boundary Integral Equations

For the derivation of the boundary integral equations, Green's second formula in Laplace domain is recalled

$$\begin{aligned} \int_\Omega \hat{\mathbf{v}}^{*\top}(\tilde{x})\, \hat{\mathcal{L}}_{\tilde{x}} \hat{\mathbf{u}}^g(\tilde{x})\, \mathrm{d}\tilde{x} + \int_\Gamma \hat{\mathbf{v}}^{*\top}(\tilde{x})\, \hat{\mathcal{T}}_{\tilde{x}} \hat{\mathbf{u}}^g(\tilde{x})\, \mathrm{d}s_{\tilde{x}} = \int_\Gamma \left(\hat{\mathcal{T}}^*_{\tilde{x}} \hat{\mathbf{v}}^*\right)^\top(\tilde{x})\, \hat{\mathbf{u}}^g(\tilde{x})\, \mathrm{d}s_{\tilde{x}} + \\ \int_\Omega \left(\hat{\mathcal{L}}^*_{\tilde{x}} \hat{\mathbf{v}}^*\right)^\top(\tilde{x})\, \hat{\mathbf{u}}^g(\tilde{x})\, \mathrm{d}\tilde{x}\,, \end{aligned} \tag{4}$$

where $\hat{\mathcal{T}}^*_{\tilde{x}}$ is defined as the Neumann trace related to the adjoint operator $\hat{\mathcal{L}}^*_{\tilde{x}}$

$$\hat{\mathcal{L}}^*_{\tilde{x}} := \begin{bmatrix} \mathcal{L}^s_{\tilde{x}} + s^2(\rho - \beta\rho^f) & -s(\alpha-\beta)\nabla_{\tilde{x}} \\ -(\alpha-\beta)\nabla^\top_{\tilde{x}} & \frac{\beta}{s\rho^f}\mathcal{L}^f_{\tilde{x}} + \frac{s\phi^2}{R} \end{bmatrix} \qquad \hat{\mathcal{T}}^*_{\tilde{x}} := \begin{bmatrix} \mathcal{T}^s_{\tilde{x}} & s\alpha \mathbf{n}_x \\ -\beta \mathbf{n}_x^\top & \frac{\beta}{s\rho^f}\frac{\partial}{\partial \mathbf{n}_{\tilde{x}}} \end{bmatrix}. \tag{5}$$

Replacing $\mathbf{v}^*(\tilde{x})$ in (4) by the adjoint fundamental solution

$$\hat{\mathbf{U}}^*(r) = \begin{bmatrix} \hat{\mathbf{U}}^s(r) & \hat{\mathbf{U}}^f(r) \\ \left(\hat{\mathbf{P}}^s\right)^\top(r) & \hat{P}^f(r) \end{bmatrix} \quad \text{with} \quad r := |y - \tilde{x}| \tag{6}$$

yields the representation formula related to the homogeneous BVP (1)

$$\hat{\mathbf{u}}^g(\tilde{x}) = (\hat{\mathcal{V}}\hat{\mathbf{t}}^g)_\Omega(\tilde{x}) - (\hat{\mathcal{W}}\hat{\mathbf{u}}^g)_\Omega(\tilde{x}) \qquad \forall \tilde{x} \in \Omega \tag{7}$$

with

$$(\hat{\mathcal{V}}\hat{\mathbf{t}}^g)_\Omega(\tilde{x}) = \int_\Gamma \hat{\mathbf{U}}^{*\top}(\tilde{x},y)\,\hat{\mathbf{t}}^g(y)\,\mathrm{d}s_y$$
$$(\hat{\mathcal{W}}\hat{\mathbf{u}}^g)_\Omega(\tilde{x}) = \int_\Gamma \left(\hat{\mathcal{T}}_y^*\hat{\mathbf{U}}^*\right)^\top(\tilde{x},y)\,\hat{\mathbf{u}}^g(y)\,\mathrm{d}s_y\,.$$

Taking the Dirichlet trace $\Omega \ni \tilde{x} \to x \in \Gamma$ and the Neumann trace $\hat{\mathcal{T}}_{\tilde{x}\to x}$ of (7) to the boundary yields the first and the second boundary integral equation, respectively

$$(\hat{\mathcal{V}}\hat{\mathbf{t}}^g)_\Gamma(x) - (\mathcal{C}+\hat{\mathcal{K}})_\Gamma\hat{\mathbf{u}}^g(x) = 0 \qquad \forall x \in \Gamma \tag{8}$$
$$(-I+\mathcal{C}+\hat{\mathcal{K}}')_\Gamma\hat{\mathbf{t}}^g(x) + (\hat{\mathcal{D}}\hat{\mathbf{u}}^g)_\Gamma(x) = 0 \qquad \forall x \in \Gamma\,, \tag{9}$$

with all the boundary integral operators defined by

$$\text{SLP} := (\hat{\mathcal{V}}\hat{\mathbf{t}}^g)_\Gamma(x) = \lim_{\Omega\ni\tilde{x}\to x\in\Gamma}\int_\Gamma \hat{\mathbf{U}}^{*\top}(\tilde{x},y)\,\hat{\mathbf{t}}^g(y)\,\mathrm{d}s_y$$
$$\text{DLP} := (\hat{\mathcal{K}}\hat{\mathbf{u}}^g)_\Gamma(x) = \lim_{\Omega\ni\tilde{x}\to x\in\Gamma}\int_\Gamma \left(\hat{\mathcal{T}}_y^*\hat{\mathbf{U}}^*\right)^\top(\tilde{x},y)\,\hat{\mathbf{u}}^g(y)\,\mathrm{d}s_y$$
$$\text{ADLP} := (\hat{\mathcal{K}}'\hat{\mathbf{t}}^g)_\Gamma(x) = \lim_{\Omega\ni\tilde{x}\to x\in\Gamma}\hat{\mathcal{T}}_{\tilde{x}}\int_\Gamma \hat{\mathbf{U}}^{*\top}(\tilde{x},y)\,\hat{\mathbf{t}}^g(y)\,\mathrm{d}s_y$$
$$\text{HSO} := (\hat{\mathcal{D}}\hat{\mathbf{u}}^g)_\Gamma(x) = -\lim_{\Omega\ni\tilde{x}\to x\in\Gamma}\hat{\mathcal{T}}_{\tilde{x}}\int_\Gamma \left(\hat{\mathcal{T}}_y^*\hat{\mathbf{U}}^*\right)^\top(\tilde{x},y)\,\hat{\mathbf{u}}^g(y)\,\mathrm{d}s_y\,.$$

Exchanging the traces with the integration does not cause any trouble for the SLP, which is defined as a weakly singular integral. However, for the DLP and the ADLP this would lead to a strongly- and for the HSO to a hyper-singular kernel function. To work around such problems, in section 2.3 a regularization will be presented.

2.2.2 Symmetric Variational Formulation

Finally, inserting appropriate extensions [26] of the given boundary data from (1)

$$\hat{\mathbf{u}}^g_\circ = \hat{\mathbf{u}}^g - \hat{\mathbf{g}}^D_\circ \in [H^{1/2}_\circ(\Gamma_N)]^4 \qquad \hat{\mathbf{t}}^g_\circ = \hat{\mathbf{t}}^g - \hat{\mathbf{g}}^N_\circ \in [H^{-1/2}(\Gamma_D)]^4 \tag{10}$$

into (8) and (9), the symmetric variational formulation reads as [26]:
Find $(\hat{\mathbf{u}}^g_\circ, \hat{\mathbf{t}}^g_\circ) \in [H^{1/2}_\circ(\Gamma_N)]^4 \times [H^{-1/2}(\Gamma_D)]^4$ *and* $s \in \mathbb{C}^{R+}$ *such that*

$$\begin{aligned}\langle\hat{\mathcal{V}}\hat{\mathbf{t}}^g_\circ, \mathbf{s}^g_\circ\rangle_{\Gamma_{DD}} - \langle\hat{\mathcal{K}}\hat{\mathbf{u}}^g_\circ, \mathbf{s}^g_\circ\rangle_{\Gamma_{ND}} &= \langle\left(\mathcal{C}+\hat{\mathcal{K}}\right)\hat{\mathbf{g}}^D_\circ, \mathbf{s}^g_\circ\rangle_{\Gamma_{DD}} - \langle\hat{\mathcal{V}}\hat{\mathbf{g}}^N_\circ, \mathbf{s}^g_\circ\rangle_{\Gamma_{ND}} \\ \langle\hat{\mathcal{K}}'\hat{\mathbf{t}}^g_\circ, \mathbf{w}^g_\circ\rangle_{\Gamma_{DN}} + \langle\hat{\mathcal{D}}\hat{\mathbf{u}}^g_\circ, \mathbf{w}^g_\circ\rangle_{\Gamma_{NN}} &= \langle\left(I-\mathcal{C}-\hat{\mathcal{K}}'\right)\hat{\mathbf{g}}^N_\circ, \mathbf{w}^g_\circ\rangle_{\Gamma_{NN}} - \langle\hat{\mathcal{D}}\hat{\mathbf{g}}^D_\circ, \mathbf{w}^g_\circ\rangle_{\Gamma_{DN}}\end{aligned} \tag{11}$$

holds for all $(\mathbf{w}^g_\circ, \mathbf{s}^g_\circ) \in [H^{1/2}_\circ(\Gamma_N)]^4 \times [H^{-1/2}(\Gamma_D)]^4$. *In the bilinear forms above, the first subscript (at* Γ*) identifies the boundary related to the ansatz- and the second to the test function.*

2.3 Regularization of the Hypersingular Bilinear Form

The regularization of the hyper-singular bilinear form is the crucial part in the formulation of the SGBEM. Therefore, the HSO for $|\tilde{x}-x|<\varepsilon$ is recalled in a detailed form

$$
\begin{aligned}
(\hat{\mathcal{D}}\hat{\mathbf{u}}^g_\circ)_\Gamma(\tilde{x}) &= -\hat{\mathcal{T}}_{\tilde{x}}\int_\Gamma \left(\hat{\mathcal{T}}^*_y\hat{\mathbf{U}}^*\right)^\top(\tilde{x},y)\,\hat{\mathbf{u}}^g_\circ(y)\,\mathrm{d}s_y \\
\begin{bmatrix} (\hat{\mathcal{D}}\hat{\mathbf{u}}_\circ)^s_\Gamma & (\hat{\mathcal{D}}\hat{p}_\circ)^s_\Gamma \\ (\hat{\mathcal{D}}\hat{\mathbf{u}}_\circ)^f_\Gamma & (\hat{\mathcal{D}}\hat{p}_\circ)^f_\Gamma \end{bmatrix}(\tilde{x}) &= -\begin{bmatrix} \mathcal{T}^s_{\tilde{x}} & -\alpha\mathbf{n}_x \\ s\beta\mathbf{n}_x^\top & \frac{\beta}{s\rho^f}\frac{\partial}{\partial\mathbf{n}_{\tilde{x}}} \end{bmatrix}\times \\
&\quad \int_\Gamma\left(\begin{bmatrix} \mathcal{T}^s_y & s\alpha\mathbf{n}_y \\ -\beta\mathbf{n}_y^\top & \frac{\beta}{s\rho^f}\frac{\partial}{\partial\mathbf{n}_y} \end{bmatrix}\begin{bmatrix} \hat{\mathbf{U}}^s & \hat{\mathbf{U}}^f \\ \left(\hat{\mathbf{P}}^s\right)^\top & \hat{P}^f \end{bmatrix}\right)^\top\begin{bmatrix} \hat{\mathbf{u}}_\circ \\ \hat{p}_\circ \end{bmatrix}\mathrm{d}s_y\,.
\end{aligned}
\tag{12}
$$

The procedure throughout the regularization of all parts in (12) is conceptually the same and, therefore, briefly described step by step:

- integrate $(\hat{\mathcal{D}}\hat{\mathbf{u}}^g_\circ)(\tilde{x})$ by parts to shift the derivatives with respect to y over to the ansatz function $\hat{\mathbf{u}}^g_\circ(y)$
- test $(\hat{\mathcal{D}}\hat{\mathbf{u}}^g_\circ)(\tilde{x})$ with $\mathbf{w}^g_\circ(\tilde{x})$ and perform integration by parts again to shift derivatives with respect to $\tilde{x}$ over to the test function
- the so obtained bilinear form has a weakly singular kernel function, thus taking the limit $\Omega\ni\tilde{x}\to x\in\Gamma$ and integration can be exchanged

Due to the nature of linear poroelasticity, reflected by the fundamental solution and by the Neumann traces, this procedure can be split into three subsections: The first concerns the fluid part, it essentially follows the regularization in [26], which is based on the work of Maue [17]. The second part deals with the solid part just like presented by Han [10], where original results of Kupradze [13] were used. Finally, the third subsection deals with the coupling terms.

Remark 2. *Note that for the boundary terms, resulting from integration by parts, either Γ_N has to be closed, or the Dirichlet datum must be zero on $\partial\Gamma$ (sufficient for applying integration by parts once) as it is ensured by the description given in section 2.2.2. This means that any interior/exterior domain problem can be treated without problem as long as its boundary is closed. That is not the case for a half-space, however with a proper closure of the domain (infinite boundary elements) this problem can be solved, too.*

Remark 3. *Throughout the regularization of the HSO one also obtains the regularized DLP (ADLP follows accordingly). These intermediate steps are skipped here for sake of brevity, while the reader may find them in [18] and the final result in* (31).

2.3.1 Fluid Term

For $\tilde{x}\in\Omega$, the HSO related to the fluid is given by

$$
(\hat{\mathcal{D}}\hat{p}_\circ)^f_\Gamma(\tilde{x}) = s\beta\mathbf{n}_{\tilde{x}}^\top\int_\Gamma\left(\beta\hat{\mathbf{U}}^s\mathbf{n}_y-\frac{\beta}{s\rho^f}\frac{\partial}{\partial\mathbf{n}_y}\hat{\mathbf{P}}^s\right)\hat{p}_\circ\mathrm{d}s_y+\frac{\beta}{s\rho^f}\frac{\partial}{\partial\mathbf{n}_{\tilde{x}}}\int_\Gamma\left(\beta\mathbf{n}_y^\top\hat{\mathbf{U}}^f-\frac{\beta}{s\rho^f}\frac{\partial}{\partial\mathbf{n}_y}\hat{P}^f\right)\hat{p}_\circ\mathrm{d}s_y\,,
$$

where in the second last term the Neumann trace can be pulled inside the integral, since $\hat{\mathbf{U}}^f$ is regular. After some further transformations, this leads to the following expression

$$(\hat{\mathcal{D}}\hat{p}_\circ)^f_\Gamma(\tilde{x}) = \frac{\beta}{s\rho^f}\frac{\partial}{\partial \mathbf{n}_{\tilde{x}}}\int_\Gamma\left(\frac{\beta}{s\rho^f}\frac{\partial}{\partial \mathbf{n}_y}\hat{P}^f\right)\hat{p}_\circ \mathrm{d}s_y + s\beta\mathbf{n}_{\tilde{x}}^\top\int_\Gamma\left(\beta\hat{\mathbf{U}}^s\mathbf{n}_y - 2\frac{\beta}{s\rho^f}\frac{\partial}{\partial \mathbf{n}_y}\hat{\mathbf{P}}^s\right)\hat{p}_\circ \mathrm{d}s_y\,.$$

Obviously, the last two expressions are just of $\mathscr{O}\left(r^{-1}\right)$, while exchanging order of differentiation and integration in the first term would lead to a kernel function of $\mathscr{O}\left(r^{-3}\right)$. Thus, for the regularization of the bilinear form, the same procedure as in [26, cf. Theorem 6.17] can be applied with the only difference that $\Delta\hat{P}^f$ does not vanish. After performing the limit $\Omega \ni \tilde{x} \to x \in \Gamma$, this results in

$$\begin{aligned}\langle\hat{\mathcal{D}}\hat{p}_\circ, v_\circ\rangle_\Gamma = \int_\Gamma\int_\Gamma\left(\frac{\beta}{s\rho^f}\right)^2\frac{\partial\hat{p}_\circ}{\partial \mathbf{S}_y}^\top\frac{\partial v_\circ}{\partial \mathbf{S}_x}\hat{P}^f\mathrm{d}s_x\mathrm{d}s_y + \int_\Gamma\int_\Gamma\left(\frac{\beta}{s\rho^f}\right)^2 v_\circ\mathbf{n}_x^\top\Delta\hat{P}^f\mathbf{n}_y\hat{p}_\circ\mathrm{d}s_x\mathrm{d}s_y \\ + \int_\Gamma\int_\Gamma s\beta v_\circ\mathbf{n}_x^\top\left(\beta\hat{\mathbf{U}}^s - 2\frac{\beta}{s\rho^f}\nabla_y\left(\hat{\mathbf{P}}^s\right)^\top\right)\mathbf{n}_y\hat{p}_\circ\mathrm{d}s_x\mathrm{d}s_y\,, \quad (13)\end{aligned}$$

with the *surface-curl* defined as $\frac{\partial}{\partial \mathbf{S}y} = (\mathbf{n}_y \times \nabla_y)$.

2.3.2 Solid Term

Due to the vectorial nature of the solid displacements versus the scalar fluid pressure, the regularization of this part is more involving than for the fluid. Again, to keep the presentation as concise as possible, only the specific steps to linear poroelasticity are elaborated in detail, whereas other results are recalled from literature [10, 11]. For $\tilde{x} \in \Omega$, the solid related HSO is given by

$$(\hat{\mathcal{D}}\hat{\mathbf{u}}_\circ)^s_\Gamma(\tilde{x}) = -\mathcal{T}^s_{\tilde{x}}\int_\Gamma\left(\left(\mathcal{T}^s_y\hat{\mathbf{U}}^s\right)^\top + s\alpha\hat{\mathbf{P}}^s\mathbf{n}_y^\top\right)\hat{\mathbf{u}}_\circ\mathrm{d}s_y + \alpha\mathbf{n}_{\tilde{x}}\int_\Gamma\left(\left(\mathcal{T}^s_y\hat{\mathbf{U}}^f\right)^\top + s\alpha\mathbf{n}_y^\top\hat{P}^f\right)\hat{\mathbf{u}}_\circ\mathrm{d}s_y\,,$$

which can be rearranged to the following form

$$\begin{aligned}(\hat{\mathcal{D}}\hat{\mathbf{u}}_\circ)^s_\Gamma(\tilde{x}) &= (\hat{\mathcal{D}}\hat{\mathbf{u}}_\circ)^{s_1}_\Gamma(\tilde{x}) + (\hat{\mathcal{D}}\hat{\mathbf{u}}_\circ)^{s_2}_\Gamma(\tilde{x}) + (\hat{\mathcal{D}}\hat{\mathbf{u}}_\circ)^{s_3}_\Gamma(\tilde{x}) \quad (14)\\ &= -\mathcal{T}^s_{\tilde{x}}\int_\Gamma\left(\mathcal{T}^s_y\hat{\mathbf{U}}^s_{sin}\right)^\top\hat{\mathbf{u}}_\circ\mathrm{d}s_y - \mathcal{T}^s_{\tilde{x}}\int_\Gamma\left(\mathcal{T}^s_y\hat{\mathbf{U}}^s_{reg}\right)^\top\hat{\mathbf{u}}_\circ\mathrm{d}s_y \\ &\quad - \int_\Gamma\alpha\left[\left(\left(\mathcal{T}^s_{\tilde{x}}\hat{\mathbf{U}}^f\right)\mathbf{n}_y^\top - \mathbf{n}_{\tilde{x}}\left(\mathcal{T}^s_y\mathbf{U}^f\right)^\top\right) - s\alpha\mathbf{n}_{\tilde{x}}\mathbf{n}_y^\top\hat{P}^f\right]\hat{\mathbf{u}}_\circ\mathrm{d}s_y\,,\end{aligned}$$

with $\hat{\mathbf{U}}^s_{sin}$ and $\hat{\mathbf{U}}^s_{reg}$ defined in (27). Exchanging the order of differentiation with integration in the first expression would lead to a kernel function of $\mathscr{O}\left(r^{-3}\right)$, while all other terms remain weakly singular. For the regularization of the hyper-singular expression above, the same procedure as in [10, pages 273-279] is applied. There, the Neumann trace is expressed via *surface-* and *Günter derivatives* $\mathcal{M}_y = \left(\mathbf{n}_y\nabla_y^\top\right)^\top - \mathbf{n}_y\nabla_y^\top$. This form of the trace allows to use Stokes's theorem for integration by parts to perform the regularization as explained in section 2.3. Following

this strategy and exchanging the elastic fundamental solution by the poroelastic fundamental solution, leads to a slightly more complicated result. First of all $\hat{\chi}$

$$\Delta^n \hat{\chi}(r) = \frac{1}{4\pi r}\left[\frac{k_1^{2n}\mathrm{e}^{-k_1 r}}{\left(k_2^2-k_1^2\right)\left(k_3^2-k_1^2\right)} + \frac{k_2^{2n}\mathrm{e}^{-k_2 r}}{\left(k_1^2-k_2^2\right)\left(k_3^2-k_2^2\right)} + \frac{k_3^{2n}\mathrm{e}^{-k_3 r}}{\left(k_1^2-k_3^2\right)\left(k_2^2-k_3^2\right)}\right] \qquad n=0,1,2\ldots \tag{15}$$

does not fulfill the bi-Laplace equation like in 3d-elasticity, but the *high order Helmholtz equation* [7]. Therefore, these derivatives [10, cf. 2.8-2.10] need to be modified

$$\begin{aligned}
-\left[\frac{\partial}{\partial \mathbf{n}_{\tilde{x}}}\frac{\partial}{\partial \mathbf{n}_y}\right]\Delta\hat{\chi} &= \left[\frac{\partial}{\partial \mathbf{S}_{\tilde{x}}}^{\top}\frac{\partial}{\partial \mathbf{S}_y} + \mathbf{n}_x^{\top}\mathbf{n}_y\Delta\right]\Delta\hat{\chi} \\
\nabla_{\tilde{x}}\frac{\partial}{\partial \mathbf{n}_y}\Delta\hat{\chi} &= \left[\mathcal{M}_y\nabla_{\tilde{x}} - \mathbf{n}_y\Delta\right]\Delta\hat{\chi} \\
\left[\mathcal{M}_y\mathcal{M}_{\tilde{x}} - \mathcal{M}_{\tilde{x}}\mathcal{M}_y\right]\Delta\hat{\chi} &= \left[\mathcal{M}_{\tilde{x}}\frac{\partial}{\partial \mathbf{n}_y} - \mathcal{M}_y\frac{\partial}{\partial \mathbf{n}_{\tilde{x}}} + \mathbf{n}_y\mathbf{n}_x^{\top}\Delta - \mathbf{n}_x\mathbf{n}_y^{\top}\Delta\right]\Delta\hat{\chi}\,.
\end{aligned}$$

With these results, the first term in term in (14) writes as

$$\begin{aligned}
(\hat{\mathcal{D}}\hat{\mathbf{u}}_\circ)_\Gamma^{s_1}(\tilde{x}) = &-\mu\sum_{k=1}^{3}\left(\frac{\partial}{\partial \mathbf{S}_{\tilde{x}}}\right)_k\int_\Gamma \Delta^2\hat{\chi}\left(\frac{\partial}{\partial \mathbf{S}_y}\right)_k\hat{\mathbf{u}}_\circ \mathrm{d}s_y \\
&-\mu\mathcal{M}_{\tilde{x}}\int_\Gamma\left(4\mu\hat{\mathbf{U}}_{sin}^s - 2\Delta^2\hat{\chi}\right)\mathcal{M}_y\hat{\mathbf{u}}_\circ \mathrm{d}s_y \\
&+\mu\int_\Gamma\left(\mathcal{M}_{\tilde{x}}\Delta^2\hat{\chi}\mathcal{M}_y\right)^{\top}\hat{\mathbf{u}}_\circ \mathrm{d}s_y \\
&+\mu\int_\Gamma\Delta^3\hat{\chi}\left(\frac{\lambda}{\mu}\mathbf{n}_x\mathbf{n}_y^{\top} + \mathbf{n}_y\mathbf{n}_x^{\top} + \mathbf{n}_x^{\top}\mathbf{n}_y\right)\hat{\mathbf{u}}_\circ \mathrm{d}s_y\,.
\end{aligned} \tag{16}$$

Formally, this result coincides with the one obtained by Han [10, cf. 2.11], except for the additional last line with $\Delta^3\hat{\chi}$, which can be found in (15). For better readability, the next few steps in the derivation are not given explicitly, but only described as they have been performed subsequently: For sake of efficiency, $\hat{\mathbf{U}}_{sin}^s$ in the second line of (16) is augmented to $\hat{\mathbf{U}}^s$ by adding and subtracting $\mathcal{M}_{\tilde{x}}\int_\Gamma 4\mu^2\hat{\mathbf{U}}_{reg}^s\mathcal{M}_y\hat{\mathbf{u}}_\circ \mathrm{d}s_y$. Then, together with the remaining two expressions from

(14) the entire regularized solid related bilinear form computes to

$$\begin{aligned}
\langle \hat{\mathcal{D}}\hat{\mathbf{u}}_\circ, \mathbf{w}_\circ\rangle_\Gamma =& \mu \int_\Gamma\int_\Gamma \Delta^2\hat{\chi} \sum_{k=1}^{3} \left(\frac{\partial}{\partial \mathbf{S}_x}\right)_k \mathbf{w}_\circ^\top \left(\frac{\partial}{\partial \mathbf{S}_y}\right)_k \hat{\mathbf{u}}_\circ \mathrm{d}s_y \mathrm{d}s_x \\
&+\mu \int_\Gamma\int_\Gamma \left(\mathcal{M}_x \mathbf{w}_\circ\right)^\top \left(2\Delta^2\hat{\chi} - 4\mu\hat{\mathbf{U}}^s\right) \left(\mathcal{M}_y \hat{\mathbf{u}}_\circ\right) \mathrm{d}s_y \mathrm{d}s_x \\
&+\mu \int_\Gamma\int_\Gamma \Delta^2\hat{\chi} \sum_{i,j,k=1}^{3} \left(\mathcal{M}_x\right)_{kj} \left(\mathbf{w}_\circ\right)_i \left(\mathcal{M}_y\right)_{ki} \left(\hat{\mathbf{u}}_\circ\right)_j \mathrm{d}s_y \mathrm{d}s_x \\
&+\mu \int_\Gamma\int_\Gamma \mathbf{w}_\circ^\top \Delta^3\hat{\chi} \left(\frac{\lambda}{\mu}\mathbf{n}_x\mathbf{n}_y^\top + \mathbf{n}_y\mathbf{n}_x^\top + \mathbf{n}_x^\top\mathbf{n}_y\right) \hat{\mathbf{u}}_\circ \mathrm{d}s_y \mathrm{d}s_x \\
&+ \int_\Gamma\int_\Gamma \mathbf{w}_\circ^\top \left(4\mu^2 \mathcal{M}_x \left(\mathcal{M}_y \hat{\mathbf{U}}^s_{reg}\right)^\top - \mathcal{T}^s_x \left(\mathcal{T}^s_y \hat{\mathbf{U}}^s_{reg}\right)^\top\right) \hat{\mathbf{u}}_\circ \mathrm{d}s_y \mathrm{d}s_x \\
&+\mu \int_\Gamma\int_\Gamma 2\alpha \left(\mathbf{w}_\circ^\top \left(\hat{\mathbf{U}}^f \mathbf{n}_x^\top\right)^\top \left(\mathcal{M}_y \hat{\mathbf{u}}_\circ\right) - \left(\mathcal{M}_x \mathbf{w}_\circ\right)^\top \left(\hat{\mathbf{U}}^f \mathbf{n}_y^\top\right) \hat{\mathbf{u}}_\circ\right) \mathrm{d}s_y \mathrm{d}s_x \\
&+ \int_\Gamma\int_\Gamma \mathbf{w}_\circ^\top \mathbf{n}_x \left(s\alpha^2 \hat{P}^f - \frac{2s^2\rho^f\alpha\left(\alpha-\beta\right)}{\beta}\left(\Delta - k_3^2\right)\Delta\hat{\chi}\right) \mathbf{n}_y^\top \hat{\mathbf{u}}_\circ \mathrm{d}s_y \mathrm{d}s_x \,.
\end{aligned} \tag{17}$$

This seems to be the most efficient form of the bilinear form. It requires $\hat{\mathbf{U}}^*$ and additionally $\Delta\hat{\chi}$, $\Delta^2\hat{\chi}$, $\Delta^3\hat{\chi}$, which are rather simple expressions (15). Only the kernel function in the fifth line of (17) results in a rather lengthy expression (33).

2.3.3 Coupling Terms

The coupling terms (12) are almost symmetric in $\tilde{x}$ and y

$$\left(\hat{\mathcal{D}}\hat{\mathbf{u}}_\circ\right)^f_\Gamma(\tilde{x}) = \int_\Gamma \left[-s\beta\mathbf{n}_{\tilde{x}}^\top \left(\left(\mathcal{T}^s_y \hat{\mathbf{U}}^s\right)^\top + s\alpha\hat{\mathbf{P}}^s\mathbf{n}_y^\top\right) - \frac{\beta}{s\rho^f}\frac{\partial}{\partial \mathbf{n}_{\tilde{x}}}\left(\left(\mathcal{T}^s_y \hat{\mathbf{U}}^f\right)^\top + s\alpha\mathbf{n}_y^\top \hat{P}^f\right)\right] \hat{\mathbf{u}}_\circ \mathrm{d}s_y$$

(18)

$$\begin{aligned}
\left(\hat{\mathcal{D}}\hat{p}_\circ\right)^s_\Gamma(\tilde{x}) &= \int_\Gamma \left[-\mathcal{T}^s_{\tilde{x}}\left(-\beta\hat{\mathbf{U}}^s\mathbf{n}_y + \frac{\beta}{s\rho^f}\frac{\partial}{\partial \mathbf{n}_y}\hat{\mathbf{P}}^s\right) + \alpha\mathbf{n}_{\tilde{x}}\left(-\beta\mathbf{n}_y^\top\hat{\mathbf{U}}^f + \frac{\beta}{s\rho^f}\mathcal{T}^s_y\hat{P}^f\right)\right] \hat{p}_\circ \mathrm{d}s_y \\
&= \int_\Gamma \left[\beta\left(\mathcal{T}^s_{\tilde{x}}\hat{\mathbf{U}}^s - \alpha\mathbf{n}_{\tilde{x}}\left(\hat{\mathbf{U}}^f\right)^\top\right)\mathbf{n}_y - \frac{\beta}{s\rho^f}\frac{\partial}{\partial \mathbf{n}_y}\left(\mathcal{T}^s_{\tilde{x}}\hat{\mathbf{P}}^s - \alpha\mathbf{n}_{\tilde{x}}\hat{P}^f\right)\right] \hat{p}_\circ \mathrm{d}s_y \,.
\end{aligned} \tag{19}$$

The expression inside the first brackets of (18) is identified as the solid related DLP kernel function (31), while the same holds for the the ADLP (32) in (19). Recalling remark 3, the

bilinear forms after the regularization and the limit $\tilde{x} \ni \Omega \to x \in \Gamma$ result in

$$\begin{aligned}
\langle \hat{\mathcal{D}}\hat{\mathbf{u}}_\circ, v_\circ\rangle_\Gamma = &-\int_\Gamma\int_\Gamma v_\circ s\beta\mathbf{n}_x^\top\left[\left(-\Delta^2\hat{\chi}+2\mu\left(\hat{\mathbf{U}}^s\right)^\top\right)\left(\mathcal{M}_y\hat{\mathbf{u}}_\circ\right)+\frac{\partial}{\partial\mathbf{n}_y}\Delta^2\hat{\chi}\hat{\mathbf{u}}_\circ\right]\mathrm{d}s_y\mathrm{d}s_x\\
&-\int_\Gamma\int_\Gamma v_\circ s\beta\mathbf{n}_x^\top\left(\mathcal{T}_y^s\hat{\mathbf{U}}_{reg}^s-2\mu\mathcal{M}_y\hat{\mathbf{U}}_{reg}^s+s\alpha\mathbf{n}_y\left(\hat{\mathbf{P}}^s\right)^\top\right)^\top\hat{\mathbf{u}}_\circ\mathrm{d}s_y\mathrm{d}s_x\\
&-\int_\Gamma\int_\Gamma v_\circ\left[s\mathbf{n}_y^\top\frac{\partial}{\partial\mathbf{n}_x}\left(\beta\Delta^2-\left(k_3^2\beta+k_4^2\alpha\right)\Delta+\alpha k_3^2k_4^2\right)\hat{\chi}\right]\hat{\mathbf{u}}_\circ\mathrm{d}s_y\mathrm{d}s_x\\
&-\int_\Gamma\int_\Gamma v_\circ 2\mu\frac{\beta}{s\rho^f}\left(\frac{\partial}{\partial\mathbf{n}_x}\hat{\mathbf{U}}^f\right)^\top\left(\mathcal{M}_y\hat{\mathbf{u}}_\circ\right)\mathrm{d}s_y\mathrm{d}s_x
\end{aligned} \tag{20}$$

and

$$\begin{aligned}
\langle \hat{\mathcal{D}}\hat{p}_\circ, \mathbf{w}_\circ\rangle_\Gamma = &\int_\Gamma\int_\Gamma\beta\left[\left(\mathcal{M}_x\mathbf{w}_\circ\right)^\top\left(-\Delta^2\hat{\chi}+2\mu\hat{\mathbf{U}}^s\right)+\mathbf{w}_\circ^\top\frac{\partial}{\partial\mathbf{n}_x}\Delta^2\hat{\chi}\right]\mathbf{n}_y\hat{p}_\circ\mathrm{d}s_y\mathrm{d}s_x\\
&+\int_\Gamma\int_\Gamma\mathbf{w}_\circ^\top\beta\left(\mathcal{T}_y^s\hat{\mathbf{U}}_{reg}^s-2\mu\mathcal{M}_x\hat{\mathbf{U}}_{reg}^s-\alpha\mathbf{n}_x^\top\left(\hat{\mathbf{U}}^f\right)^\top\right)\mathbf{n}_y\hat{p}_\circ\mathrm{d}s_y\mathrm{d}s_x\\
&+\int_\Gamma\int_\Gamma\mathbf{w}_\circ^\top\left[\mathbf{n}_x\frac{\partial}{\partial\mathbf{n}_y}\left(\beta\Delta^2-\left(k_3^2\beta+k_4^2\alpha\right)\Delta+\alpha k_3^2k_4^2\right)\hat{\chi}\right]\hat{p}_\circ\mathrm{d}s_y\mathrm{d}s_x\\
&-\int_\Gamma\int_\Gamma 2\mu\frac{\beta}{s\rho^f}\left(\mathcal{M}_x\mathbf{w}_\circ\right)^\top\left(\frac{\partial}{\partial\mathbf{n}_x}\hat{\mathbf{P}}^s\right)\hat{p}_\circ\mathrm{d}s_y\mathrm{d}s_x
\end{aligned} \tag{21}$$

accordingly.

3 Symmetric Time Domain Galerkin Boundary Element Method

The time domain problem statement in terms of a symmetric variational boundary integral formulation follows from a formal inverse Laplace transformation of (11):
Find $\left(\mathbf{u}_\circ^g, \mathbf{t}_\circ^g\right)$ *such that*

$$\begin{aligned}
\langle\mathcal{V}*\mathbf{t}_\circ^g,\mathbf{s}_\circ^g\rangle_{\Gamma_{DD}}-\langle\mathcal{K}*\mathbf{u}_\circ^g,\mathbf{s}_\circ^g\rangle_{\Gamma_{ND}} &= \langle(\mathcal{C}+\mathcal{K})*\mathbf{g}_\circ^D,\mathbf{s}_\circ^g\rangle_{\Gamma_{DD}}-\langle\mathcal{V}*\mathbf{g}_\circ^N,\mathbf{s}_\circ^g\rangle_{\Gamma_{ND}}\\
\langle\mathcal{K}'*\mathbf{t}_\circ^g,\mathbf{w}_\circ^g\rangle_{\Gamma_{DN}}+\langle\mathcal{D}*\mathbf{u}_\circ^g,\mathbf{w}_\circ^g\rangle_{\Gamma_{NN}} &= \langle\left(I-\mathcal{C}-\mathcal{K}'\right)*\mathbf{g}_\circ^N,\mathbf{w}_\circ^g\rangle_{\Gamma_{NN}}-\langle\mathcal{D}*\mathbf{g}_\circ^D,\mathbf{w}_\circ^g\rangle_{\Gamma_{DN}}
\end{aligned} \tag{22}$$

holds for all $\left(\mathbf{w}_\circ^g, \mathbf{s}_\circ^g\right)$.

3.1 Temporal Discretization

Here, exactly the same version of the CQM [1] as explained in [18] is applied. How this method is used to decouple the time domain variational form (22) into a set of Laplace domain ones (11), is exemplary shown on the first bilinear form in (22)

$$\langle\mathcal{V}*\mathbf{t}_\circ^g,\mathbf{s}_\circ^g\rangle_{\Gamma_{DD}}(t)=\int_0^t\int_{\Gamma_D}\mathbf{s}_\circ^{g\top}(x)\int_{\Gamma_D}\mathbf{U}^{*\top}(x-y,t-\tau)\,\mathbf{t}_\circ^g(y,\tau)\,\mathrm{d}s_y\mathrm{d}s_x\mathrm{d}\tau\,.$$

Splitting the time interval $(0,t)$ into $M+1$ equidistant time steps Δt the convolution at a discrete time-step $t_n = n\Delta t$ may be approximated by

$$\begin{aligned}\langle \mathcal{V} * \mathbf{t}^g_\circ, \mathbf{s}^g_\circ \rangle_{\Gamma_{DD}}(t_n) &\approx \sum_{\ell=0}^{M} \frac{\mathscr{R}^{-n}}{M+1} \int_{\Gamma_D} \mathbf{s}^{g\top}_\circ(x) \int_{\Gamma_D} \hat{\mathbf{U}}^{*\top}(x-y,s_\ell)\, \hat{\mathbf{t}}^g_\circ(y,s_\ell)\, \mathrm{d}s_y \mathrm{d}s_x \zeta^{\ell n} \\ &\approx \sum_{\ell=0}^{M} \frac{\mathscr{R}^{-n}}{M+1} \langle \hat{\mathcal{V}} \hat{\mathbf{t}}^g_\circ(s_\ell), \mathbf{s}^g_\circ \rangle_{\Gamma_{DD}} \zeta^{\ell n} \end{aligned} \tag{23}$$

with

$$\hat{\mathbf{t}}^g_\circ(s_\ell) = \sum_{k=0}^{M} \mathscr{R}^k \mathbf{t}_\circ(t_k)\, \zeta^{-\ell k}, \quad s_\ell = \frac{\gamma\left(\mathscr{R}\zeta^{-\ell}\right)}{\Delta t} \quad \text{and} \quad \zeta = \mathrm{e}^{\frac{2\pi \mathrm{i}}{M+1}},$$

where $\mathscr{R}$ is the radius of a circle lying in the domain of analyticity of the kernel function and $\gamma(z)$ the quotient of the characteristic polynomials of the underlying linear multistep method incorporated in the CQM. Applying this technique to all expressions in (22) leads to a set of $M+1$ decoupled Laplace domain problems to be discretized in space. Note that the CQM in the original version would lead to exactly the same results.

3.2 Spatial Discretization

Due to the reasoning in the previous section a spatial discretization of (11), i.e. the SG variational formulation of an elliptic system, is sufficient. This is done in a standard fashion by introducing a triangulation of the boundary

$$\Gamma_h = \Gamma_{D,h} \cup \Gamma_{N,h} = \bigcup_{k=1}^{K} \bar{\tau}_k$$

on which the unknown Cauchy data (10) are approximated

$$\begin{aligned}(\hat{\mathbf{u}}^g_{\circ,h})_k(x) &= \sum_{i=1}^{n_N} \hat{\mathrm{u}}_{\circ,i} \varphi^1_i(x) \quad \in S^1_{\circ,h}(\Gamma_{N,h}) := \mathrm{span}\{\varphi^1_i\}_{i=1}^{n_N} \subset H^{1/2}_\circ(\Gamma_{N,h}) \quad k = 1\ldots 4 \\ (\hat{\mathbf{t}}^g_{\circ,h})_k(x) &= \sum_{k=1}^{n_D} \hat{\mathrm{t}}_{\circ,i} \psi^0_i(x) \quad \in S^0_{\circ,h}(\Gamma_{D,h}) := \mathrm{span}\{\psi^0_i\}_{i=1}^{n_D} \subset H^{-1/2}(\Gamma_{D,h}) \quad k = 1\ldots 4\,. \end{aligned}$$

$S^1_{\circ,h}$ is the trial space of piecewise linear and continuous basis functions φ^1_i and $S^0_{\circ,h}$ of piecewise constant basis functions ψ^0_i. This leads to a set of discrete systems for a fixed s_ℓ

$$\begin{bmatrix} \hat{\mathsf{V}} & -\hat{\mathsf{K}} \\ \hat{\mathsf{K}}' & \hat{\mathsf{D}} \end{bmatrix}_\ell \begin{bmatrix} \hat{\mathrm{t}}_\circ \\ \hat{\mathrm{u}}_\circ \end{bmatrix}_\ell = \begin{bmatrix} \hat{\mathsf{f}}_\mathsf{D} \\ \hat{\mathsf{f}}_\mathsf{N} \end{bmatrix}_\ell \qquad \ell = 0\ldots M \tag{24}$$

where the right hand side is defined in (11). The discrete system is component wise given by, e.g. the single layer matrix

$$\hat{\mathrm{V}}[k,j] = \langle \hat{\mathcal{V}} \psi^0_j, \psi^0_k \rangle_{\Gamma_{DD,h}} = \int\limits_{\mathrm{supp}\left(\psi^0_k\right)} \psi^0_k(x) \int\limits_{\mathrm{supp}\left(\psi^0_j\right)} \hat{\mathbf{U}}^{*\top}(x,y,s_\ell)\, \psi^0_j(y)\, \mathrm{d}s_y \mathrm{d}s_x \quad k,j = 1\ldots n_D\,.$$

Due to the regularization of all bilinear forms for the numerical computation of all matrices a weakly singular quadrature rule based on Duffy transformation [20] is sufficient. A GMRES is used to solve (24) via Schur complement. Within this scheme, the SLP is preconditioned by a BPX and the HSO by a coarsely computed SLP. Finally, from these solutions time domain results are obtained through (23).

4 Numerical Examples

All results were obtained by using the HyENA C++ library for solving partial differential equations using boundary element methods [19]. For the approximation of the Dirichlet data piecewise linear and continuous elements while for the Neumann data piecewise constant elements were used. Moreover, for the linear multistep method involved within the CQM, the BDF2 was chosen. Which effect other choices of multistep methods have on the CQM is reported in [2].

Table 1: Material properties of rock (Berea sandstone) [12]

	$\lambda\,[\mathrm{N/m^2}]$	$\mu\,[\mathrm{N/m^2}]$	$\rho\,[\mathrm{kg/m^3}]$	$\phi\,[-]$	$\alpha\,[\mathrm{N/m^2}]$	$\rho^f\,[\mathrm{kg/m^3}]$	$R\,[\mathrm{N/m^2}]$	$\kappa\,[\mathrm{m^4/Ns}]$
rock	0	$7.2\cdot 10^9$	2458	0.19	0.778	1000	$4.885\cdot 10^8$	$1.9\cdot 10^{-10}$

For all computations the material data of Berea sandstone (see Table1) is used. Note that $\lambda = 0\,\mathrm{N/m^2}$ results from setting Poisson's ratio to zero. This modification was introduced for the one dimensional wave propagation example, with the intention to reduce three dimensional effects.

4.1 One Dimensional Wave Propagation – Column

In this section, one dimensional wave propagation is studied with the presented SGBEM formulation. The results are compared with the semi-analytic solution [23] and the CBEM results of the authors themselves [18]. The aim is to show the behavior with respect to different spatial, respectively, temporal discretization and, finally, also to have a look at the long time behavior in terms of numerical stability.

The problem under consideration is sketched in Figure1, where a poroelastic column of 3 m length and a cross-sectional area of $1\,\mathrm{m}^2$ is depicted. At $x_3 = 3\,\mathrm{m}$ this column is subjected to a negative stress unit step-load in the longitudinal direction and zero stress in both transverse directions as well as zero pressure. To come as close as possible to the one dimensional case, all other faces are supported by impermeable roller bearings, i.e. out of plane displacements are zero and vice versa for the stresses. Furthermore, as the name implies, no flux through the sidewalls is allowed.

For sake of comparison the same meshes are used for both methods: MESH0 in Figure2(a) consists of 56 elements and 30 nodes, MESH1 in Figure2(b) consists of 224 elements and 114 nodes, MESH2 in Figure2(c) has 896 elements and 540 nodes and MESH3 in Figure2(d) 3584 elements and 1794 nodes. In the following COL*i*/GAL*i* refers to the CBEM/SGBEM results related to MESH*i* for $i = 0\ldots 3$. Furthermore, for the characterization of the temporal discretization, the

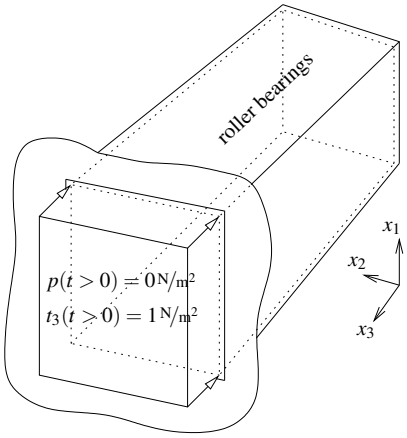

Figure 1: Poroelastic column with roller bearing support

Cournant-Friedrichs-Levy number

$$\beta_{\mathrm{CFL}} = \frac{c_1 \Delta t}{h} \tag{25}$$

is used, with the limit of the fast compression wave speed c_1 for $t \to 0$, the time step Δt and the mesh size h defined by the triangle's longest side. Corresponding to the prescribed boundary conditions, the following results are looked at: Solid displacement u_3 and fluid flux q at the center of the top face at $x_3 = 3\,\mathrm{m}$; solid stress t_3 and fluid pressure p in the middle of the bottom face at $x_3 = 0\,\mathrm{m}$. In all figures, the continuous lines correspond to the SGBEM results while the dotted lines are related to the CBEM results. Note that the results belonging to the coarsest mesh are not plotted in the following figures for sake of clarity, but it is just used for the comparison in Table2.

Different spatial discretizations at a constant $\beta_{\mathrm{CFL}} = 0.3$ are compared in Figure3. These results have two things in common: First, one can observe that the finer the mesh, the better the coincidence between both methods, e.g. in Figure3(a) the result for the coarsest mesh (COL1/GAL1) differs at the kinks, while almost no difference is visible when looking at the finest discretization (COL3/GAL3). The stress and pressure plots are omitted, since they behave similarly, while when looking at the flux results in Figure3(b) the advantage of the SGBEM becomes most obvious. Secondly, one can observe less numerical damping in the SGBEM's results, i.e. the difference in the displacement results in Figure3(a) differs more the later in time they are observed. Finally, to conclude this study, point wise relative L_2 errors in time between these results and the semi-analytic solution are computed and reported in Table2, e.g. for the solid displacement result COL0 this is

$$L_2^{\mathrm{COL0}}(u) := \sqrt{\frac{\int_0^t \left[u^{\mathrm{COL0}}(\tau) - u_h(\tau)\right]^2 \mathrm{d}\tau}{\int_0^t \left[u^{\mathrm{COL0}}(\tau)\right]^2 \mathrm{d}\tau}}\,. \tag{26}$$

When looking at these results, one should keep in mind that the one dimensional solution is not the exact reference solution corresponding to the three dimensional BEM computations.

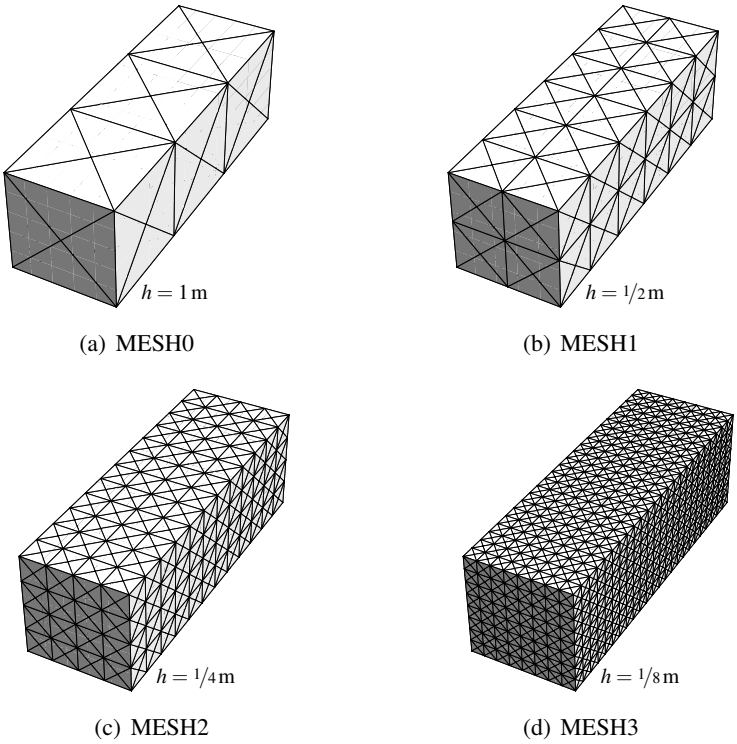

(a) MESH0 (b) MESH1

(c) MESH2 (d) MESH3

Figure 2: Different spatial discretizations of the considered column

Hence, once the error drops below a certain level, it may even rise again. This is most likely the explanation for the behavior of the SGBEM in the last level, except of the flux, where this bound has not been reached, yet.

Table 2: Point wise relative L_2 errors

MESH	displacement		stress		pressure		flux	
	CBEM	SGBEM	CBEM	SGBEM	CBEM	SGBEM	CBEM	SGBEM
0	4.75e-02	1.10e-02	6.71e-02	3.86e-03	6.89e-02	5.66e-03	8.02e-01	9.71e-02
1	2.43e-02	1.79e-03	3.74e-02	1.73e-03	3.93e-02	1.94e-03	5.63e-01	2.44e-02
2	6.64e-03	8.41e-04	1.86e-02	1.68e-03	1.86e-02	1.72e-03	3.64e-01	7.23e-03
3	1.82e-03	3.06e-03	9.97e-03	4.34e-03	9.67e-03	4.33e-03	1.99e-01	4.54e-03

Different temporal discretizations are compared in Figure4 by varying the β_{CFL} factor for the intermediate spatial discretization (MESH2). While a proper relation of time-step to mesh size was used in the previous study, here less optimal choices are investigated. At a to coarse time step ($\beta_{\mathrm{CFL}} = 0.8$) both methods give almost identical results (see Figure4(a) and Figure4(b)), while the CBEM becomes unstable at an earlier stage than the SGBEM, as can be seen in the

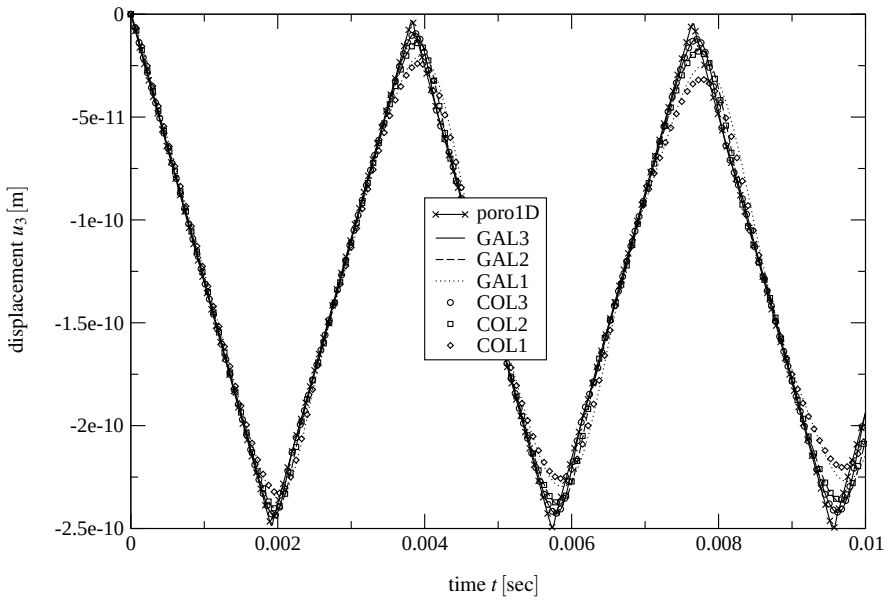

(a) solid displacement u_3

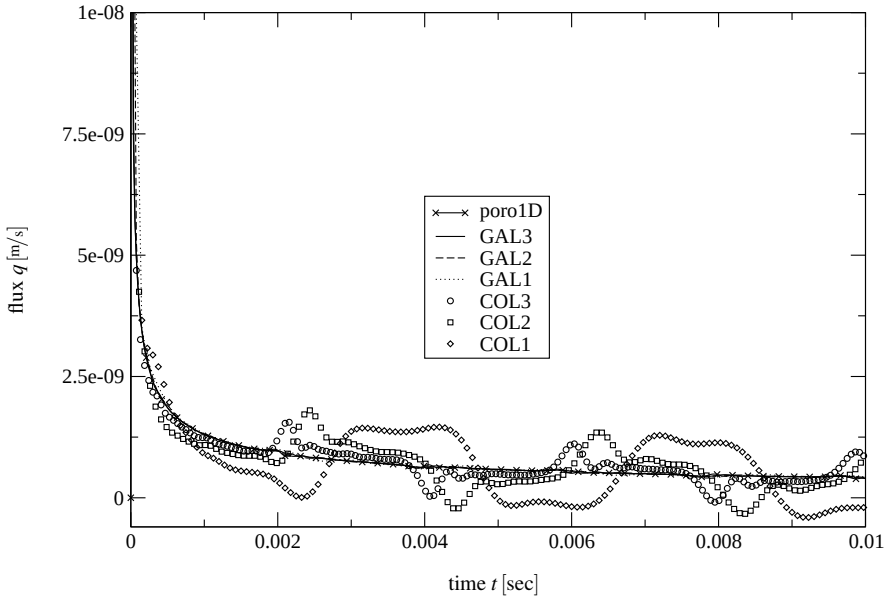

(b) fluid flux q

Figure 3: Results at $x_3 = 0\,\mathrm{m}$ for different spatial discretizations ($\beta_{\mathrm{CFL}} = 0.3$)

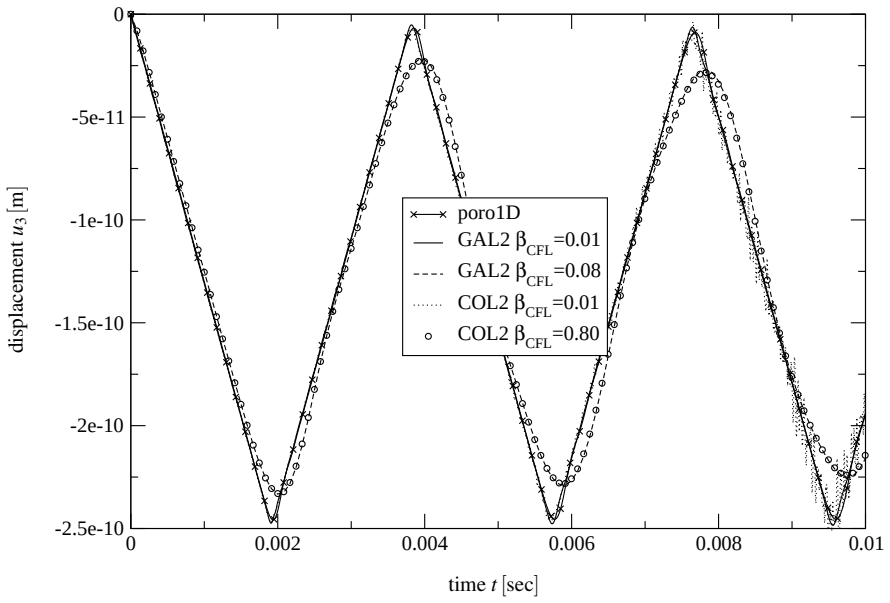

(a) displacement u_3

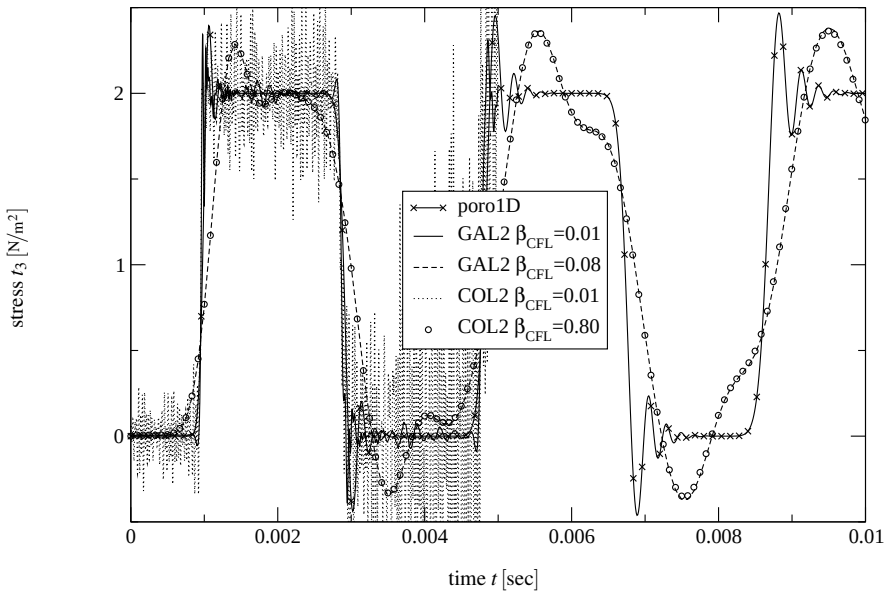

(b) stress t_3

Figure 4: Results for fixed spatial- COL2/GAL2 and different temporal discretizations

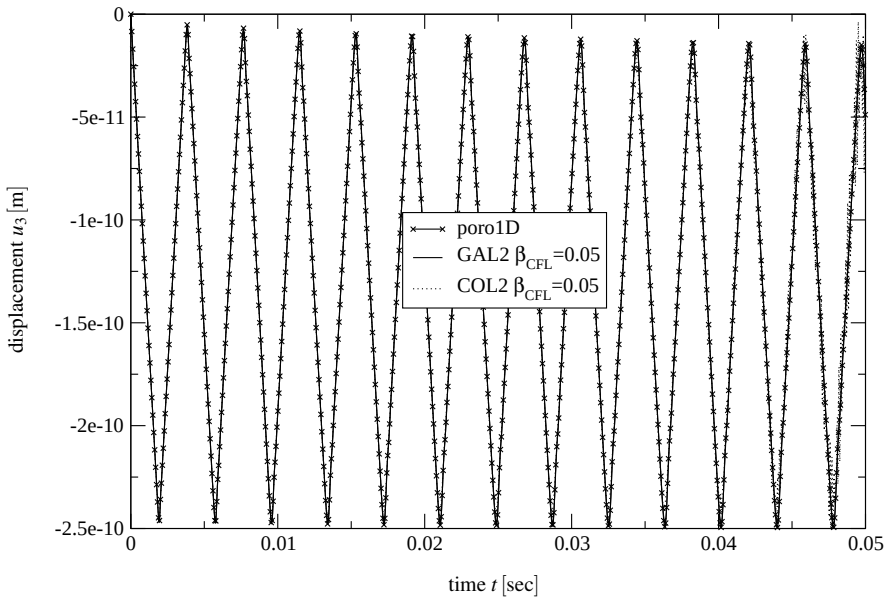

(a) displacement u_3

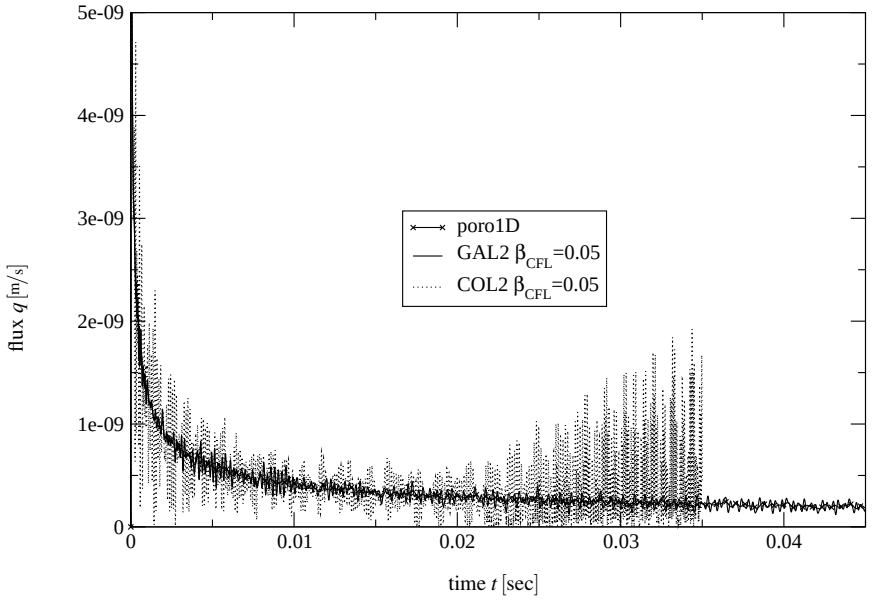

(b) flux q

Figure 5: Long time stability of COL2/GAL2 at $\beta_{\mathrm{CFL}} = 0.05$

displacement as well as in the stress results at $\beta_{\text{CFL}} = 0.01$. Similar observations can be made for the two remaining field variables, the fluid pressure behaves like the solid stress and the flux even worse, which plots are omitted for sake of brevity.

Long time stability behavior is studied in Figure5. To show the SGBEM's advantages over the CBEM, the previous two comparisons suggest to perform this study with a rather fine time step. Thus, in the following MESH2 with a β_{CFL} of 0.05 is used. With this configuration, the SGBEM has a clear advantage in terms of long time stability. The SGBEM's displacement results remain completely stable in Figure5(a), while the CBEM becomes unstable after some time. Skipping the corresponding plots for sake of space, the same holds for the solid stress and fluid pressure, where this problem on the CBEM's side becomes a little more evident. Finally, for this time-step, the fluid flux results delivered by the CBEM are completely unstable from the beginning on (for sake of better readability they are only plotted up to $t = 0.035\,\text{sec}$), while the SGBEM performs quite a bit better, even though it also oscillates around the reference solution, see Figure5(b).

4.2 Spatial Convergence Rates – Cube

Unfortunately, the convergence study in Table2 is not covered by the theory. On one hand this is due to the non smooth right hand side and on the other hand due to the point wise spatial observation. However, Schanz et al. [24] proved the operator (2) to be coercive. Thus, it can be shown that for the SGBEM formulation the same convergence rates as, e.g. for the Laplace equation [26] follow. The time discretization for the SGBEM formulation presented in this paper is identical with the one in the CBEM formulation presented in [18], i.e. time domain results are obtained from a set of Laplace domain problems. Having this fact in mind, it is assumed to be sufficient to look at the convergence rates for some constant Laplace parameters to point out the differences between the two spatial discretizations.

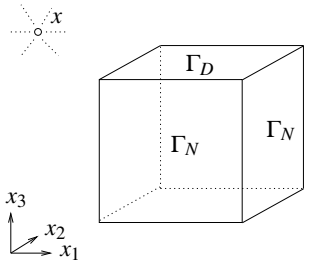

Figure 6: A unit cube is subjected to the fundamental solution on Γ_D (top and bottom face) and its Neumann trace on Γ_N (surrounding faces), while x is fixed at some exterior point

On a unit cube (Figure6), the last row of the fundamental solution ($\hat{\mathbf{U}}^f$, $\hat{P}^f$) is prescribed on the Dirichlet boundary and its Neumann trace on the Neumann boundary, each time with the load point x fixed at some distance outside the unit cube, hence the given boundary data are C^∞. Such a BVP has an analytic solution, i.e. the fundamental solution itself and its Neumann trace on the complementary boundaries.

Starting from the coarsest spatial discretization with two triangles per face in level 0, the mesh is uniformly refined in the subsequent levels. In the following, the relative L_2 errors of the SGBEM and the CBEM computations are compared in Table3 and Table4 for $s_\ell = (1,1)$. Such studies have been performed for different values of s_ℓ with just slightly varying outcome, i.e. for such a regular right hand side, both methods seem to perform more or less equally well.

Table 3: SGBEM relative L_2 errors for $s_\ell = (1,1)$

level	displacement $\frac{\|u-u_h\|_{L_2}}{\|u\|_{L_2}}$	rate	pressure $\frac{\|p-p_h\|_{L_2}}{\|p\|_{L_2}}$	rate	stress $\frac{\|t-t_h\|_{L_2}}{\|t\|_{L_2}}$	rate	flux $\frac{\|q-q_h\|_{L_2}}{\|q\|_{L_2}}$	rate
0	4.44e-01		2.18e-01		3.32e-01		2.80e-01	
1	1.33e-01	1.74	6.73e-02	1.70	1.99e-01	0.74	1.99e-01	0.50
2	3.86e-02	1.78	1.70e-02	1.99	1.01e-01	0.97	9.93e-02	1.00
3	1.06e-02	1.86	4.15e-03	2.03	5.08e-02	1.00	4.94e-02	1.01
4	2.80e-03	1.92	1.02e-03	2.02	2.54e-02	1.00	2.46e-02	1.01
5	7.17e-04	1.97	2.55e-04	2.01	1.27e-02	1.00	1.22e-02	1.00

Table 4: CBEM relative L_2 errors for $s_\ell = (1,1)$

level	displacement $\frac{\|u-u_h\|_{L_2}}{\|u\|_{L_2}}$	rate	pressure $\frac{\|p-p_h\|_{L_2}}{\|p\|_{L_2}}$	rate	stress $\frac{\|t-t_h\|_{L_2}}{\|t\|_{L_2}}$	rate	flux $\frac{\|q-q_h\|_{L_2}}{\|q\|_{L_2}}$	rate
0	3.25e-0		2.27e-01		3.29e-01		2.79e-01	
1	8.93e-0	1.86	8.23e-02	1.46	1.97e-01	0.74	1.95e-01	0.51
2	2.81e-0	1.67	2.40e-02	1.78	1.01e-01	0.96	9.86e-02	0.99
3	8.18e-0	1.78	6.14e-03	1.97	5.08e-02	0.99	4.94e-02	1.00
4	2.30e-0	1.83	1.51e-03	2.02	2.55e-02	0.99	2.49e-02	0.99
5	6.42e-0	1.84	3.74e-04	2.02	1.31e-02	0.96	1.32e-02	0.91

5 Conclusion

A symmetric Galerkin Boundary Element Method for linear poroelasticity based on regularized kernels has been presented.

The convergence behavior on some benchmark problems has been shown and compared with a collocation method. It seems that for problems where the mathematical theory fully applies, the collocation method reaches the performance of the symmetric Galerkin method. However, this was not really confirmed by the more practical example, where one dimensional wave propagation due to a step load was studied. There, the SGBEM performs better than the collocation BEM, with the most drastic difference in the flux results. This observation holds for an ideal space/time discretization. In the case of a not optimal relation between mesh and time-step size the SGBEM has clear advantages over the collocation BEM, which can also be observed in terms of long time stability for rather fine time discretization.

An important remark on infinite domains: The presented approach does not violate the far field conditions, it only requires the closure of the domain. The half-space does not work right

away within this framework, since it does not include the boundary terms resulting from the application of Stokes's theorem (remark 2). These contributions are strictly due to the open domain in the discrete setting, on which the Dirichlet data are unknown. With the here presented approach it seems that the classical truncation does not work because the error due to the truncation becomes too big. However, treating the boundary's infinite extent via e.g. infinite boundary elements would solve this problem. A further remark concerning this point: In the second example the source point x could have been placed inside the unit cube without additional efforts (exterior domain problem) resulting in the very same convergence rates.

Finally one should remark on the computation time: For the convergence study in Laplace domain the factor CBEM/SGBEM is about $1/10$. One has to consider that for the SGBEM approach double integration is required, compared to just single integration as in the CBEM approach and additionally, the second BIE is much more expensive to evaluate compared to the first BIE as it is the case in the CBEM formulation. Last but not least, when looking at the one dimensional wave propagation example the time factor becomes even worse. The simple explanation is that the second boundary integral equation seems to be more sensitive to the non smooth data on the right hand side, i.e. the entries must be computed with a much higher accuracy, leading to a longer computation time in comparison to the CBEM.

Even though it may seem like the SGBEM's drawbacks are not balanced by its benefits, this formulation definitely has its advantages, when it comes to a symmetric coupling with FEM. This is an important point, when it comes to realistic applications.

Acknowledgement The authors gratefully acknowledge the financial support of the Austrian Science Fund (FWF) within the *Doktoratskolleg W1208 – Numerical Simulations in Technical Science*.

A Appendix

A.1 Poroelastodynamic Fundamental Solution

The adjoint Laplace domain fundamental solution

$$\hat{\mathbf{U}}^*(r) = \begin{bmatrix} \hat{\mathbf{U}}^s(r) & \hat{\mathbf{U}}^f(r) \\ \left(\hat{\mathbf{P}}^s\right)^\top(r) & \hat{P}^f(r) \end{bmatrix} = \begin{bmatrix} \mathscr{O}(r^{-1}) & \mathscr{O}(r^0) \\ \mathscr{O}(r^0) & \mathscr{O}(r^{-1}) \end{bmatrix} \quad \text{with} \quad r := |y-x|$$

is defined by the following terms

$$\begin{aligned} \hat{\mathbf{U}}^s(r) =& \hat{\mathbf{U}}^s_{sin}(r) + \hat{\mathbf{U}}^s_{reg}(r) \\ =& \frac{1}{\mu}\left[\Delta\mathbf{I} - \left(\frac{\lambda+\mu}{\lambda+2\mu}\right)\nabla\nabla^\top\right]\Delta\hat{\chi}(r) \qquad (27) \\ & - \frac{1}{\mu}\left[\left(\Delta(k_1^2+k_2^2) - k_1^2k_2^2\right)\mathbf{I} - \left(k_1^2+k_2^2-k_4^2-\frac{k_1^2k_2^2}{k_3^2}\right)\nabla\nabla^\top\right]\hat{\chi}(r) \qquad (28) \\ P^f(r) =& \frac{s\rho^f}{\beta}\Delta^2\hat{\chi}(r) - \frac{s\rho^f}{\beta}\left(\left(k_3^2+k_4^2\right)\Delta - k_3^2k_4^2\right)\hat{\chi}(r) \qquad (29) \end{aligned}$$

$$\hat{\mathbf{P}}^s(r) = \frac{\hat{\mathbf{U}}^f}{s} = -\frac{s\rho^f}{\beta}\frac{\alpha-\beta}{\lambda+2\mu}\nabla_y\left(\Delta - k_3^2\right)\hat{\chi}(r) \tag{30}$$

where k_1, k_2, and k_3 are the wave numbers related to the fast/slow compressional, and the shear wave [21], whereas the abbreviation $k_4 = k_3\sqrt{\mu/\lambda+2\mu}$ is just introduced for notational convenience.

A.2 Regularized Adjoint/Double Layer Bilinear Forms

The regularized solid related bilinear form for the DLP is given by

$$\langle\hat{\mathcal{K}}\hat{\mathbf{u}}_\circ, \mathbf{s}_\circ\rangle_\Gamma^s = \int_\Gamma\int_\Gamma \mathbf{s}_\circ^\top\Big[\left(-\Delta_{\mathbf{y}}^2\hat{\chi} + 2\mu\hat{\mathbf{U}}_\circ^s\right)\left(\mathcal{M}_{\mathbf{y}}\hat{\mathbf{u}}_\circ\right) + \left(\frac{\partial}{\partial\mathbf{n}_y}\Delta_{\mathbf{y}}^2\hat{\chi}\right)\hat{\mathbf{u}}_\circ + \left(\left(\mathcal{T}_y^s - 2\mu\mathcal{M}_y\right)\hat{\mathbf{U}}_{reg}^s + \alpha\hat{\mathbf{U}}^f\mathbf{n}_y^\top\right)^\top\hat{\mathbf{u}}_\circ\Big]\mathrm{d}s_y\mathrm{d}s_x \tag{31}$$

while for the ADLP it is

$$\langle\hat{\mathcal{K}}'\hat{\mathbf{t}}_\circ, \mathbf{w}_\circ\rangle_\Gamma^s = \int_\Gamma\int_\Gamma\Big[\left(\mathcal{M}_x\mathbf{w}_\circ\right)^\top\left(-\Delta^2\hat{\chi} + 2\mu\hat{\mathbf{U}}^s\right) + \mathbf{w}_\circ^\top\left(\frac{\partial}{\partial\mathbf{n}_x}\Delta^2\hat{\chi}\right) + \hat{\mathbf{w}}_\circ^\top\left(\left(\mathcal{T}_x^s - 2\mu\mathcal{M}_x\right)\hat{\mathbf{U}}_{reg}^{s\top} - \alpha\mathbf{n}_x\hat{\mathbf{U}}^{f\top}\right)\Big]\hat{\mathbf{t}}_\circ\mathrm{d}s_x\mathrm{d}s_y\,. \tag{32}$$

A.3 Part of the HSO bilinear form kernel function

$$\begin{aligned}
&\left[4\mu^2\mathcal{M}_x\left(\mathcal{M}_y\hat{\mathbf{U}}_{reg}^s\right)^\top - \mathcal{T}_x^s\left(\mathcal{T}_y^s\hat{\mathbf{U}}_{reg}^s\right)^\top\right]_{\ell k} = \sum_{i,j=1}^{3}\left(4\mu^2\left(\mathcal{M}_x\right)_{i\ell}\left(\mathcal{M}_y\right)_{kj} - \left(\mathcal{T}_x^s\right)_{\ell i}\left(\mathcal{T}_y^s\right)_{kj}\right)\left(\hat{\mathbf{U}}_{reg}^s\right)_{ij}\\
&= \frac{\left(4\mu^2-\lambda^2\right)}{\mu}\sum_{i,j=1}^{3}\left[\left(k_4^2 + \frac{k_1^2k_2^2}{k_3^2}\right)\frac{\partial^2}{\partial^2 y_i} - k_1^2k_2^2\right]n_\ell^x n_k^y\frac{\partial^2\hat{\chi}}{\partial^2 y_j}\\
&- \frac{\left(4\mu^2+2\lambda\mu\right)}{\mu}\sum_{i,j=1}^{3}\left[\left(k_4^2 + \frac{k_1^2k_2^2}{k_3^2}\right)\frac{\partial^2}{\partial^2 y_i} - k_1^2k_2^2\right]\left(n_\ell^x n_j^y\frac{\partial^2\hat{\chi}}{\partial y_j\partial y_k} + n_j^x n_k^y\frac{\partial^2\hat{\chi}}{\partial y_j\partial y_\ell}\right)\\
&- \mu\sum_{i,j,t=1}^{3}\left[\left(k_1^2+k_2^2\right)\frac{\partial^2}{\partial^2 y_i} - k_1^2k_2^2\right]\left(n_k^x n_j^y\frac{\partial^2\hat{\chi}}{\partial y_\ell\partial y_j} + n_j^x n_\ell^y\frac{\partial^2\hat{\chi}}{\partial y_j\partial y_k} + \delta_{\ell k}n_t^x n_j^y\frac{\partial^2\hat{\chi}}{\partial y_j\partial y_t} - 3n_j^x n_j^y\frac{\partial^2\hat{\chi}}{\partial y_\ell\partial y_k}\right)
\end{aligned} \tag{33}$$

References

[1] L. Banjai and S. Sauter. Rapid solution of the wave equation in unbounded domains. *Journal on Numerical Analysis*, 47(1):227–249109–128, 2008.

[2] L. Banjai and M. Schanz. Wave propagation problems treated with convolution quadrature and BEM. In U. Langer, M. Schanz, O. Steinbach, and W. L. Wendland, editors, *Fast Boundary Element Methods in Engineering and Industrial Applications*, chapter 5, pages 147–187. Springer, 2012.

[3] M. A. Biot. Theory of propagation of elastic waves in a fluid-saturated porous solid. I. *Journal of the Acoustical Society of America*, 28(2):168–178, 1956.

[4] M. A. Biot. Theory of propagation of elastic waves in a fluid-saturated porous solid. II. *Journal of the Acoustical Society of America*, 28(2):179–191, 1956.

[5] G. Bonnet. Basic singular solutions for a poroelastic medium in the dynamic range. *Journal of the Acoustical Society of America*, 82(5):1758–1763, 1987.

[6] M. Bonnet, G. Maier, and C. Polizzotto. Symmetric Galerkin boundary element method. *Applied Mechanics Review*, 51:669–704, 1998.

[7] A. H.-D. Cheng. On Free Space Green's Function for Higher Order Helmholtz Equations. In *Boundary Element Methods: Fundamentals and Applications*, Proceedings of the IABEM Symposium, Kyoto, 1991.

[8] M. Costabel and E. P. Stephan. Coupling of finite and boundary element methods for an elastoplastic interface problem. *SIAM Journal on Numerical Analysis*, 27(5):1212–1226, 1990.

[9] M. Guiggiani, G. Krishnasamy, T. J. Rudolphi, and F. J. Rizzo. A general algorithm for the numerical solution of hypersingular boundary integral equations. *Journal of Applied Mechanics*, 59(3):604–614, 1992.

[10] H. Han. The boundary integro-differential equations of three-dimensional Neumann problem in linear elasticity. *Numerische Mathematik*, 68:268–281, 1994.

[11] L. Kielhorn and M. Schanz. Convolution quadrature method-based symmetric Galerkin boundary element method for 3-d elastodynamics. *International Journal for Numerical Methods in Engineering*, 76:1724–1746, 2008.

[12] Y. K. Kim and H. B. Kingsbury. Dynamic characterization of poroelastic materials. *Experimental Mechanics*, 19:252–258, 1979.

[13] V. D. Kupradze. *Three-dimensional problems of the mathematical theory of elasticity and thermoelasticity*. North-Holland, 1979.

[14] C. Lubich. Convolution quadrature and discretized operational calculus I. *Numerische Mathematik*, 52:129–145, 1988.

[15] C. Lubich. Convolution quadrature and discretized operational calculus II. *Numerische Mathematik*, 52:413–425, 1988.

[16] G. D. Manolis and D. E. Beskos. Integral formulation and fundamental solutions of dynamic poroelasticity and thermoelasticity. *Acta Mechanica*, 76:89–104, 1989.

[17] A. W. Maue. Zur Formulierung eines allgemeinen Beugungsproblems durch eine Integralgleichung. *Zeitschrift für Physik*, 126(7-9):609–618, 1949.

[18] M. Messner and M. Schanz. A regularized collocation boundary element method for linear poroelasticity. *Computational Mechanics*, 47:669–680, 2011.

[19] M. Messner, M. Messner, F. Rammerstorfer, and P. Urthaler. Hyperbolic and Elliptic Numerical Analysis BEM library. http://www.mech.tugraz.at/HyENA, 2010.

[20] S. Sauter and C. Schwab. *Boundary Element Methods*. Springer, 2010.

[21] M. Schanz. *Wave Propagation in Viscoelastic and Poroelastic Continua*, volume 2 of *Lecture Notes in Applied Mechanics*. Springer, 2001.

[22] M. Schanz. Poroelastodynamics: Linear Models, Analytical Solutions, and Numerical Methods. *Applied Mechanics Review*, 62(3):030803–1–030803–15, 2009.

[23] M. Schanz and A. H. D. Cheng. Transient wave propagation in a one-dimensional poroelastic column. *Acta Mechanica*, 145:1–18, 2000.

[24] M. Schanz, O. Steinbach, and P. Urthaler. A boundary integral formulation for poroelastic materials. *PAMM*, 9(1):595–596, 2009.

[25] S. Sirtori, G. Maier, G. Novati, and S. Miccoli. A Galerkin symmetric boundary-element method in elasticity: Formulation and implementation. *International Journal for Numerical Methods in Engineering*, 35(2):255–282, 1992.

[26] O. Steinbach. *Numerical Approximation Methods for Elliptic Boundary Value Problems*. Springer, 2008.

[27] T. Wiebe and H. Antes. A time domain integral formulation fo dynamic poroelasticity. *Acta Mechanica*, 90:125–137, 1991.